

1    **Predictive Wear Modelling of the Articulating Metal-on-Metal Hip**

2    **Replacements**

3

4    Leiming Gao<sup>1\*</sup>, Duncan Dowson<sup>2</sup>, Robert W. Hewson<sup>1</sup>

5

6    <sup>1</sup>Aeronautics Department, Imperial College London, SW7 2AZ, UK

7    <sup>2</sup>School of Mechanical Engineering, University of Leeds, LS2 9JT, UK

8    \*[leiming.gao@imperial.ac.uk](mailto:leiming.gao@imperial.ac.uk)

9    [r.hewson@imperial.ac.uk](mailto:r.hewson@imperial.ac.uk)

10   [d.dowson@leeds.ac.uk](mailto:d.dowson@leeds.ac.uk)

# **Predictive Wear Modelling of the Articulating Metal-on-Metal Hip**

## **Replacements**

### **Key words**

Wear model; elastohydrodynamic lubrication (EHL); metal-on-metal total hip joint replacement; Archard law; numerical simulation

### **Abstract**

The lubrication regime in which artificial hip joints operate adds complexity to the prediction of wear, as the joint operates in both the full fluid film regime, specifically the elastohydrodynamic lubrication (EHL) regime, and the mixed or boundary lubrication regimes, where contact between the bearing surfaces results in wear. In this work a wear model is developed which considers lubrication for the first time via a transient EHL model of metal-on-metal hip replacements. This is a framework to investigate how the change in film thickness influences the wear, which is important to further investigation of the complex wear procedure, including tribo-corrosion, in the lubricated hip implants. The wear model applied here is based on the work of Sharif et al. who adapted the Archard wear law by making the wear rate a function of a relative film thickness nominalized by surface roughness for examining wear of industrial gears. In this work the gait cycle employed in hip simulator tests is computationally investigated and wear is predicted for two sizes of metal-on-metal total hip replacements. The wear results qualitatively predict the typical wear curve obtained from experimental hip simulator tests, with an initial 'running-in period' before a lower wear rate is reached. The shape of the wear scar has been simulated on both the acetabular cup and femoral head bearing surfaces.

# 1 Introduction

2 The prediction of wear in hip replacements has been a subject of intense study in recent  
3 years. Such a predictive capability has proved difficult to achieve because of the competing  
4 and complex physics at play in the artificial joint. The joint operates in both the full fluid film  
5 regime, specifically the Elastohydrodynamic Lubrication (EHL) regime, as well as the mixed  
6 or even boundary lubrication regime, where contact between the artificial femoral head and  
7 the acetabula cup leads to wearing of the opposing surfaces, a full predictive description of  
8 the problem is challenging. It is this transition from one lubrication regime to the other as  
9 well as a description of wear in the mixed lubrication regime which presents significant  
10 challenges to the predictive modelling process.

11 A significant amount of research has been undertaken on the EHL of artificial hip joints.<sup>1-</sup>  
12 <sup>13</sup> In these models the interaction of the fluid film pressure and the elastically deformable  
13 head and cup are calculated to predict both the film thickness and the lubricating fluid  
14 pressure. Such studies have shown that the fluid filled lubricating gap is at nanometre size –  
15 an extremely small gap when compared to typical engineering bearing problems, where the  
16 fluid filled gap is typically in a range of (1-100)  $\mu\text{m}$ .<sup>14, 15</sup>

17 Compared with the ideal spherical bearing geometry, the non-spherical geometries of  
18 bearing surfaces, which may be a result of wear, affect the gap between the cup and head  
19 surfaces (clearances) and consequently affect lubrication<sup>16-18</sup> and wear. The change of  
20 bearing geometry during wear resulting in a decreased contact pressure was also observed  
21 in the EHL studies of hip implants<sup>19</sup>, such that the peak pressure was reduced and pressure  
22 was distributed more evenly on the bearing surface. However, some wear models, in which  
23 lubrication is not explicitly incorporated, predicted a constant wear rate (for a fixed wear  
24 coefficient) although they may also predict a decreased contact pressure as the bearing

1 geometry changed during wear. This has included work using a finite element approach to  
2 calculate the local dry contact pressure, which is then used as the basis for the wear  
3 calculations.<sup>20-26</sup> When the Archard wear law<sup>27</sup> has been applied to this problem a linear  
4 wear volume per cycle is obtained as the total force applied to the joint is the same resulting  
5 in the integration of the wear volume over the surface being constant. As such the predicted  
6 wear rate does not replicate the trends observed experimentally in the simulator tests.

7 The wear results obtained from artificial hip simulators typically show an initial “running  
8 in period” for approximately 1 to 2 million cycles, before a lower wear rate is reached  
9 (Figure 1). This “classical” wear trend<sup>28</sup> is followed for the majority of cases; however, there  
10 are some notable exceptions, which include cases of runaway wear and breakaway wear  
11 where a low steady wear rate may not be obtained. The reasons for these cases are possibly  
12 due to adverse loading and motion conditions and needs further study. This “classical”  
13 experimental trend has been observed in both metal-on-plastic (cobalt-chrome on  
14 UHMWPE) joints, metal-on-metal joints<sup>29</sup> as well as joints where one or both surfaces are  
15 ceramic. This is despite the significantly different wear rates observed for the different  
16 bearing surface materials or different gait cycles ranging from simplified patterns to more  
17 realistic physiological patterns.<sup>30-35</sup> The role of head geometry has been examined for both  
18 total hip replacement and hip resurfacing,<sup>14, 25</sup> with the effect of the head radius on the  
19 wear rate examined, it was shown experimentally that under conditions that avoided edge  
20 wear, a trend was shown for lower wear with larger head radius implants.

21 Wear particles and ion release attributed to metal-on-metal total hip replacements<sup>36, 37</sup>  
22 and the associated health problems<sup>38-40</sup> have resulted in the number of this type of hip  
23 replacement being used less.<sup>41, 42</sup> In the early to mid-1990’s the wear of polyethylene cups  
24 was implicated in early device failure and morbidity.<sup>43</sup> Despite the potential biocompatible

issues associated with metal elements some MoM hip implants have exhibited encouraging tribological and clinical performance.

The challenging problem of wear modelling when a fluid film is present has been investigated outside the field of artificial joint modelling. This includes the work of Sharif et al.<sup>44</sup> who developed a wear model for gears. In their model the predicted wear depends on a relative fluid film thickness nominated by surface roughness, and the sensitivity of wear rate to the relative film thickness is controlled by a power term which was obtained empirically. However, the same limitations of the Archard wear model are also present in the adapted wear model when it is applied on a conforming contact rather than a sliding point contact for which it was developed.

A similar approach is used in this work to produce the first model capable of predicting total hip replacement wear in the presence of a full fluid film. The aim of the study is to outline the framework required to simulate lubrication and wear in a hip joint, and to highlight the importance of including both of these if the “typical” wear predictions are to be replicated computationally. The model results provide the potential to apply optimisation to the design of joint geometry to reduce surface wear and its resulting debris.

## **Materials and Methods**

### ***Wear model***

Modelling of wear of MOM hip replacements which operate in a lubricated regime is clearly dependent on the film thickness. The wear rate of the implant bearing surfaces was described using an adapted Archard wear formula<sup>44</sup> in which the effect of both fluid pressure and film thickness is considered:

$$wear\ rate = k_w p v \left( \frac{R_a}{h} \right)^a \quad (1)$$

where  $k_w$  is the dimensional wear coefficient,  $p$  is the fluid pressure,  $R_a$  is composite surface roughness,  $h$  is the fluid film thickness, and  $v$  is the local relative sliding speed between the two surfaces.

The power term ( $a$ ) determines how abruptly the transition to wear occurs with a decreasing film thickness and its value is based on the value obtained by Sharif et al.<sup>44</sup>, the result of which is that the wear model does not need to change during the wear process. The effect of this power term ( $a$ ) and film thickness on a non-dimensional wear rate [ $W_L/(k_w p v)$ ] is illustrated (Figure 2), given the same wear coefficient, load, speed and surface roughness. This will be discussed in the Results Section. The linear wear at an arbitrary point ( $i, j$ ) on the bearing surfaces at the  $k^{\text{th}}$  time step in one gait cycle can be derived as

$$W_L^{i,j}(k) = k_w p_{i,j} v_{i,j} \Delta t \left( \frac{R_a}{h_{i,j}} \right)^a \quad (2)$$

where,  $\Delta t$  is the discrete time step. After the calculation of all time steps ( $n$ ), the wear depth in one cycle at point ( $i, j$ ) was summed as

$$W_{L\_cycle}^{i,j} = \sum_{k=1}^n W_L^{i,j}(k) \quad (3)$$

The total wear depth at point ( $i, j$ ) after  $N$  cycles is calculated approximately as the number of cycles times the wear depth per cycle, if the surface profile does not change much within  $N$  cycles. After a certain number of cycles the surface geometry changes are large enough to affect the pressure and film thickness, then the surface profile needs to be updated for the lubrication simulation, new pressures and film thicknesses are obtained and used to calculate the following cycles. As shown in Eq. (4), the wear coefficient and number of cycles (i.e. time) can be grouped together, which indicates that the wear coefficient can

be ‘scaled’ with time and make the predicted wear ‘independent’ from the wear coefficient.

This will be illustrated clearly in the results.

$$W_{L\_total}^{i,j} = \sum_1^N W_{L\_cycle}^{i,j} \approx N \cdot \sum_{k=1}^n \left[ k_w p_{i,j} v_{i,j} \Delta t \left( \frac{R_a}{h_{i,j}} \right)^a \right]$$

$$\approx (N \cdot k_w) \sum_{k=1}^n \left[ p_{i,j} v_{i,j} \Delta t \left( \frac{R_a}{h_{i,j}} \right)^a \right] \quad (4)$$

The local relative sliding speed was calculated as

$$v = \sqrt{v_\theta^2 + v_\varphi^2} \quad (5)$$

$$\begin{cases} v_\theta = -R \omega_x \sin \varphi + R \omega_y \cos \varphi \\ v_\varphi = -R \omega_x \cos \varphi \cos \theta - R \omega_y \sin \varphi \cos \theta + R \omega_z \sin \theta \end{cases} \quad (6)$$

where,  $\varphi$  and  $\theta$  are spherical coordinates;  $\omega_x$ ,  $\omega_y$ ,  $\omega_z$  represent the angular velocities of flexion-extension, internal-external rotation and adduction-abduction respectively.

For each mesh point, the volumetric wear was calculated as a product of the linear wear and the area of the mesh cell with that point as vertex. The area of each mesh cell on the spherical surface was approximated as the area of a trapezoid as the curvature is small enough compared to the cup radius.

The flowchart describing the wear simulation procedure is given (Figure 3). The geometry change of bearing surfaces due to wear was updated with a fixed interval frequency of every 100,000 cycles. As will be demonstrated, this updating frequency provides independent wear results when realistic wear coefficients are applied.

### ***EHL model***

The Reynolds equation was used to describe the lubricated flow between the cup and head surfaces, formulated in spherical coordinates.<sup>1, 7</sup>

1

2

$$\begin{aligned}
& \frac{\partial}{\partial \varphi} \left( h^3 \frac{\partial p}{\partial \varphi} \right) + \sin \theta \frac{\partial}{\partial \theta} \left( h^3 \sin \theta \frac{\partial p}{\partial \theta} \right) \\
& = 6\eta R^2 \sin \theta \left[ -\omega_x \left( \sin \varphi \sin \theta \frac{\partial h}{\partial \theta} + \cos \varphi \cos \theta \frac{\partial h}{\partial \varphi} \right) \right. \\
& \quad \left. + \omega_y \left( \cos \varphi \sin \theta \frac{\partial h}{\partial \theta} - \sin \varphi \cos \theta \frac{\partial h}{\partial \varphi} \right) \right. \\
& \quad \left. + \omega_z \sin \theta \frac{\partial h}{\partial \varphi} \right] \\
& \quad + 12\eta R^2 \sin^2 \theta \frac{\partial h}{\partial t}
\end{aligned} \tag{7}$$

3

4

5

6

7

8

9

10

11

The synovial fluid was assumed to be incompressible and have a constant viscosity ( $\eta$ ) of 0.0009 Pas at high shear rate of approximately  $10^7 \text{ s}^{-1}$ .<sup>45, 46</sup> The role of shear thinning fluids is therefore likely to have a role in determining the level of wear predicted, as it has been shown to play a role in dictating the minimum film thickness.<sup>47</sup> Other constituents of synovial fluid, such as absorbed protein layers may also play a role in EHL and wear.<sup>48, 49</sup> These are something which requires more investigation and may result in greater quantitative agreement between experimental results and the model presented here. Given the initial angle ( $\beta$ ) of the inclined cup, the inlet and outlet boundaries of the lubricated domain were defined as:

12

$$\begin{cases} \theta_{in} = 0, \theta_{out} = \pi \\ \varphi_{in} = \beta, \varphi_{out} = \beta + \pi \end{cases} \tag{8}$$

13

14

15

16

The hydrodynamic pressure ( $p$ ) was assumed to be zero at both the inlet and the outlet boundaries defined by Eq. (8). The cavitation boundary condition was achieved by setting the obtained negative pressure of zero during the relaxation process in the entire calculation domain.

17

18

The film thickness ( $h$ ) including both rigid and elastic deformation ( $\delta$ ) between the two bearing surfaces, was calculated as



$$h(\varphi, \theta) = c - e_x \sin \theta \cos \varphi - e_y \sin \theta \sin \varphi - e_z \cos \theta + \delta(\varphi, \theta) \quad (9)$$

$$\delta(\varphi, \theta) = \int_{\varphi} \int_{\theta} K(\varphi - \varphi', \theta - \theta', \theta_m) p(\varphi', \theta') d\theta' d\varphi' \quad (10)$$

An equivalent spherical discrete convolution (ESDC) technique<sup>50</sup> and the multi-level multi-integration (MLMI)<sup>51</sup> were adopted to obtain the surface elastic deformation.  $K$  denotes the influence coefficient of the elastic surfaces and  $\theta_m$  denotes a fixed mean latitude<sup>50</sup>.

It may be noted that the EHL solver used is able to deal with mixed lubrication conditions with zero film thickness numerically predicted at some points in the computing domain. To avoid infinite value of the exponential term ( $R_d/h$ ) in the wear Eq. (1), a minimum gap was adopted<sup>44</sup>. In this paper the minimum gap was set as  $h_0 = 20$  nm which is in the range of the measured boundary film layer in MoM hip replacements<sup>52</sup>, and the value is chosen with consideration of numerical convergence. During the iterations, if the calculated film thickness from Eq. (9) was below  $h_0$  at certain point, the boundary film thickness Eq. (11), in which the film thickness was set to 20 nm, was used to calculate the elastic deformation ( $\delta$ ). Then the pressure at that point was calculated from the elastic deformation using Eq. (10) with pressures at all other points known.

$$h_0 = c - e_x \sin \theta \cos \varphi - e_y \sin \theta \sin \varphi - e_z \cos \theta + \delta(\varphi, \theta) \quad (11)$$

The external 3D loading components  $f_x, f_y, f_z$  were balanced by the hydrodynamic pressure integrated with respect to the corresponding axes:

$$f_{x,y,z} = R^2 \int_{\varphi} \int_{\theta} p_{x,y,z} d\theta d\varphi \quad (12)$$

where the pressure components in three Cartesian coordinate directions are expressed as:

$$\begin{cases} p_x = p \sin^2 \theta \cos \varphi \\ p_y = p \sin^2 \theta \sin \varphi \\ p_z = p \sin \theta \cos \theta \end{cases} \quad (13)$$

The governing equations were made dimensionless in order to improve numerical stability and facilitate convergence, by introducing the following scaling parameters:<sup>7</sup>

$$P = \frac{p}{E}, H = \frac{h}{c}, \Delta = \frac{\delta}{c}, F_{x,y,z} = \frac{f_{x,y,z}}{ER^2}, \varepsilon = \frac{c^2 E \cdot H^3}{6\eta R^2 \omega_0},$$

$$\Omega_{x,y,z} = \omega_{x,y,z} / \omega_0, T = t \cdot \omega_0, \bar{e}_{x,y,z} = e_{x,y,z} / c \quad (14)$$

where  $\omega_0$  can be any constant except zero. The equations were subsequently transformed into discrete forms using the finite difference schemes. Gauss-Seidel relaxation was employed for pressure iteration in the Reynolds equation, and the Multi-Grid techniques<sup>51</sup> were employed with the maximum mesh grid of 256×256. The numerical procedure used to solve the lubrication equations is the same as that in reference.<sup>7</sup>

### ***Geometry, materials and loading profiles***

The metal-on-metal total hip replacement was investigated with two sizes of femoral head and clearance: (i) 28-mm head diameter (briefly noted as Head 28) with 40 μm diametrical clearance; (ii) 36-mm head diameter (briefly noted as Head 36) with 50 μm diametrical clearance. The clearance values are typical of those used in simulator studies<sup>14</sup>, allowing comparison with the trends found in the published literature to be made. The composite surface roughness of 40 nm of the cup and head bearing surfaces was employed.<sup>28, 34, 53, 54</sup> The cup was assumed to be firmly fixed to the pelvic bone through an equivalent layer representing bone and/or fixation cement.<sup>8</sup> The material and geometrical parameters are presented in Table 1. An illustration of the hip implant with applied loading and motions is shown (Figure 4). The loading and motion patterns of gait cycles employed in Leeds II (ProSim) hip simulator was considered in this study (Figure 5), composed of one load and two motions, flexion-extension and internal-external rotation, and no internal-

external rotation, i.e.  $\omega_z = 0$ . There were  $n = 100$  time steps in the total cyclic time of one second. The inclination angle of cup was set to 45 degrees.<sup>14</sup> In the present study micro-separation was not considered.

## Results

A range of different wear coefficients were investigated for Head 36 bearing with a fixed power term ( $a$ ) of 2.24 in Figure 6. The solid curve shows the wear prediction of 12 million cycles using wear coefficient of  $k_w = 1 \times 10^{-9} \text{mm}^3/(\text{Nm})$ ; the 'dot' curve shows 6 million cycles using  $k_w = 2 \times 10^{-9} \text{mm}^3/(\text{Nm})$ ; the 'cross' curve shows 4 million cycles using  $k_w = 3 \times 10^{-9} \text{mm}^3/(\text{Nm})$ . These wear coefficient values are in agreement with literatures which ranged from  $1 \times 10^{-9}$  to  $1 \times 10^{-8} \text{mm}^3/(\text{Nm})$ .<sup>22, 23, 25</sup> The predicted wear is plotted as a function of the product of time (number of cycles) and wear coefficient, which is shown in the bracket in Eq. (4). The reason this scaling has been used is that if the wear is updated frequently enough, then all the lines will coincide as doubling the wear factor will have exactly the same effect as doubling the number of cycles. Confirming that these wear results coincide is therefore a good demonstration of an appropriate wear update rate and the reason why 0.1 million cycles was chosen as the update frequency of the joint wear.

A value of 2.24 for the power term ( $a$ ) in the wear Eq. (1) was found to reasonably capture surface wear by Sharif et al.,<sup>44</sup> although the different geometry and surface characteristics may result in a different value being more appropriate, requiring further investigation. In the current study a range of values 1, 2 and 2.24 of the power term were used for comparisons (Figure 7). Dowson (2006)<sup>33</sup> obtained a relationship for the global wear volume as a function of the minimum film thickness and it is interesting to note that

the factor used in this work is of a similar magnitude as that used in Dowson's global approximation (1.49). The non-linear trend in the predicted wear has been found more obviously with a higher value of the power term.

For the rest of the results, the power term was fixed to 2.24 and the wear coefficient was fixed to  $1 \times 10^{-9} \text{mm}^3/(\text{Nm})$ . For both Head 36 and Head 28, wear simulations were completed for 15 million cycles. Separate wear on cup and head surfaces are shown in [Figure 8 (A) and (B)] for Head 36 hip implants, and [Figure 8 (C) and (D)] for Head 28 respectively. In order to present the non-linear wear trend in Figure 8 clearly, the wear rate are listed in Table II for both Head 36 and Head 28 hip bearings. The wear rate (wear volume per million cycles) was calculated as the difference in the accumulated wear between the beginning and the end of each million cycles. The percentage was calculated based on that of the first million cycles. For example, for Head 28, the wear rate was reduced significantly from  $0.0302 \text{ mm}^3/\text{million cycle}$  in the first million cycle to  $0.0099 \text{ mm}^3/\text{million cycle}$  (32.8% of that in the 1<sup>st</sup> million cycle) after 12 million cycles, and became more stable at  $0.0085 \text{ mm}^3/\text{million cycle}$  (28.1%) after 15 million cycles. It is also observed that the accumulated wear on the cup and head surfaces are very similar to each other, while the maximum wear depth shows a more substantial difference.

The development of wear scar (wear profile contours at selected time intervals, 8 and 15 million cycles) for the cup and head surface is presented in Figure 9 for the Head 36 joint bearing. The time averaged pressure and film thickness at the central cross-section [illustrated as the dash line in Figure 4] of the cup bearing surface are plotted in Figure 10. The value of pressure or film thickness at each mesh point was averaged through the cyclic gait time. It illustrated how the distribution of pressure and gap changed due to change of surface profile before and after wear.

## Discussion

Despite the simplicity of the wear model and constant wear coefficient assumed in the wear components of the model, a classic wear result for the artificial hip is produced computationally by including EHL effects, resulting in a single wear coefficient, rather needing to apply an initial bedding-in wear coefficient followed by a steady one. Such an approach can capture the general trend alludes to the importance of including the fluid lubrication regime in determining the underlying physics of the problem. Two wear stages were obtained, the bedding-in stage within the first few million cycles where the wear rate is higher, followed by the steady-state wear stage where the wear rate is reduced significantly (approximately 50% to 70% reduced) (Figure 8A and C, and Table II). Although this result is not as dramatic as those sometimes encountered in experimental testing we believe the non-linear wear rate we have demonstrated provides a significant route to explain why the mixed lubrication regime is so important and points to potential future developments which could be taken in developing more advanced mixed lubrication wear models to improve the correlation further.

The reduced wear rate is attributable to the change in the surface profile, which resulting in a decrease in pressure in the thin film lubricated area. The change in the surface profile as a result of the surface wear effectively make the head and cup geometries of a more similar radius, increased the loading area, increased the local gap and decreased the peak pressures. This can be seen from the time averaged pressure and film thickness distribution (Figure 10), which representing the averaged load and motion situations in gait cycle. With the effect of lubrication considered the current wear model is able to capture the non-linear wear that practically occurs.

1 It is interesting to observe that although the wear volume of the head and cup is the  
2 same – as would be assumed from the wear model which assumes the same wear rate for  
3 the head and cup – the maximum wear depth is not the same for the two hip bearing  
4 surfaces (Figure 8). This is because of the transient nature of the wear process and where it  
5 occurs on the head and cup, leading to different shaped wear scars (Figure 9). The wear scar  
6 on head surfaces of Head 28 clearly showed a double lobed shape (Figure 9D) as observed in  
7 hip simulator studies under the same motion conditions (flexion-extension and internal-  
8 external rotation).<sup>55</sup>

9 The accumulated wear volume of Head 36 was found to be lower than that of Head 28,  
10 approximately by 30% ( $0.12 \text{ mm}^3$  versus  $0.17 \text{ mm}^3$ ) [Figure 8 (A) and (C)]. This trend is  
11 consistent with the experimental work<sup>14, 34</sup> that larger diameter implants resulted in lower  
12 wear. The non-linear property in the predicted wear rate is mainly determined by the  
13 surface roughness ( $R_a$ ) and the power term ( $\alpha$ ) in the wear formula. Before wear, the cyclic  
14 minimum film thickness ranged in (22-37) nm for Head 28 implant, while the corresponding  
15 values for Head 36 was much larger ranged in (30-47) nm. The cyclic central film thickness  
16 ranged in (38-49) nm with an average value of 44 nm for Head 28; the corresponding values  
17 for Head 36 are ranged in (47-66) nm with an average value of 58 nm. If the cyclic central  
18 film thicknesses are compared, it can be seen in Figure 2 that the dimensionless wear rate  
19  $[W_L/(k_w p v)]$  at 44 nm (corresponding to Head 28) was approximately twice of that at 58 nm  
20 (corresponding to Head 36). Therefore, the larger film thickness in Head 36, resulted in a  
21 lower wear rate with same surface roughness ( $R_a$ ) considered. However, the current  
22 simulation was based on a single statistical surface roughness parameter, the real measured  
23 surface roughness need to be further studied.

The predicted wear rate is lower than that typically obtained from hip simulators<sup>14</sup> (of the order of 0.01 mm<sup>3</sup> versus 0.1 mm<sup>3</sup> per million cycles simulated). However, the predicted wear is able to be ‘scaled’ against time if the wear coefficient is ‘scaled’, as proved in Figure 6, and therefore it is arbitrarily chosen, informed by approximate values. If the wear coefficient is enlarged by 10 times, the predicted wear in 15 million cycles could be plotted as the same curve against time axis of 1.5 million cycles, which will give a 10 times higher wear rate than the current. This highlighted that the preliminary model is able to predict the reduced wear rate against time even using a linear wear formula in which the wear rate is linear with the wear coefficient and load.

This coupling of the level of wear to that of the wear rate, via the change in film thickness has been demonstrated and shown to reproduce the general wear trends encountered experimentally. There is significant scope to enhance such a model through the inclusion of shear thinning properties and a more comprehensive model of the mixed lubrication regime in order to reproduce better quantitative agreement between the model and those of experiments. The role of the 20 nm minimum film thickness implemented to ensure computational convergence may also be limiting the level of wear observed, highlighting a need for a more accurate model of wear and the mixed lubrication regime to capture not just the qualitative wear trends but the quantitative levels of wear experimentally observed.

## Conclusions

This study highlights the importance of including wear and lubrication in the numerical simulation of the articulating hip joint replacements. The resulting model is able to capture

1 how experimentally obtained wear rates vary with time using a linear wear model (with load  
2 and wear coefficient) and an EHL simulation of the lubrication in the joint. The gait cycle  
3 employed in hip simulator tests has been investigated and wear has been predicted for two  
4 sizes of the femoral head of metal-on-metal total hip replacements. The predicted results  
5 qualitatively show the two stage of wear bedding-in stage with higher wear rate followed by  
6 a phase with a lower wear rate. The model demonstrates the important role that a changing  
7 fluid film thickness due to wear plays on the wear process itself. The model results provide  
8 an avenue to not only further understand artificial joint wear and how the wear debris  
9 moves from where it is generated and out of the joint, but also to optimise the joint  
10 geometry to reduce rate at which wear occurs. The model described here highlights the  
11 importance of the change in film thickness on the wear process, further work is required to  
12 more accurately capture the complex mixed lubrication wear process as well as potentially  
13 including tribo-corrosion effects.

## 15 **Acknowledgement**

16 The research leading to these results has received funding from the European Union's  
17 Seventh Framework Programme (FP7/2007-2013) under the LifeLongJoints Project, Grant  
18 Agreement No. GA-310477.



# 1 Nomenclature

2

$a$	Power term in Eq. (1)	$N$	Number of gait cycles
$c$	Radial clearance between cup and head (m)	$t$	Time (s)
$e$	Eccentricity component (m)	$T$	Non-dimensional time
$\bar{e}$	Non-dimensional eccentricity component	$t_0$	Gait cyclic time (s)
$E$	Elastic modulus (Pa)	$\Delta t$	Time step, $\Delta t = t_0/n$
$f$	Applied load (N)	$v$	sliding velocity (m/s)
$F$	Non-dimensional load	$v_\theta, v_\phi$	Spherical velocity component (m/s)
$h$	Film thickness (m)	$W_L$	Linear wear at one time step (m)
$h_0$	Boundary film thickness (m)	$W_{L\_cycle}$	Linear wear in one gait cycle (m)
$H$	Non-dimensional film thickness	$W_{L\_total}$	Total linear wear (m)
$k$	Time step counter in one gait cycle	$\beta$	Angle of cup inclination (rad)
$k_w$	Wear coefficient, [mm <sup>3</sup> /(Nm)]	$\Delta$	Non-dimensional elastic deformation of surface
$K$	Influence coefficients matrix for the elastic deformation (m/N)	$\delta$	Surface elastic deformation (m)
$p$	Pressure (Pa)	$\phi, \theta$	Spherical coordinates (rad)
$P$	Non-dimensional pressure	$\eta$	Viscosity of synovial fluid (Pas)
$R_a$	Average surface roughness (m)	$\omega$	Angular velocity (rad/s)
$R$	Cup radius (m)	$\omega_0$	Scaling parameter of angular velocity (rad/s)
$n$	Total number of time steps in one gait cycle	$\Omega$	Non-dimensional angular velocity

Subscript

$x, y, z$  Cartesian coordinates

3

4

## 1    **References**

- 2    1. Meyer DM, Tichy JA. Lubrication model of an artificial hip joint: Pressure profile versus  
3    inclination angle of the acetabular cup. *Trans ASME J Tribol.* 1999;121:492-498.
- 4    2. Jin ZM. Theoretical studies of elastohydrodynamic lubrication of artificial hip joints. *Proc*  
5    *Inst Mech Eng Part J: J Eng Trib.* 2006;220:719-727.
- 6    3. Liu F, Jin ZM, Roberts P, Grigoris P. Effect of bearing geometry and structure support on  
7    transient elastohydrodynamic lubrication of metal-on-metal hip implants. *J Biomech.*  
8    2007;40:1340-1349.
- 9    4. Wang FC, Jin ZM. Transient elastohydrodynamic lubrication of hip joint implants. *Trans*  
10    *ASME J Tribol.* 2008;130:011007.
- 11    5. Wang WZ, Jin ZM, Dowson D, Hu YZ. A study of the effect of model geometry and  
12    lubricant rheology upon the elastohydrodynamic lubrication performance of metal-on-metal  
13    hip joints. *Proc Inst Mech Eng Part J: J Eng Trib.* 2008;222:493-501.
- 14    6. Meziane A, Bou-Said B, Tichy J. Modelling human hip joint lubrication subject to walking  
15    cycle. *Lubr Sci.* 2008;20:205-222.
- 16    7. Gao LM, Wang FC, Yang PR, Jin ZM. Effect of 3D physiological loading and motion on  
17    elastohydrodynamic lubrication of metal-on-metal total hip replacements. *Med Eng Phys.*  
18    2009;31:720-729.
- 19    8. Gao LM, Yang PR, Dymond I, Fisher J, Jin ZM. Effect of surface texturing on the  
20    elastohydrodynamic lubrication analysis of metal-on-metal hip implants. *Tribol Int.*  
21    2010;43:1851-1860.
- 22    9. Meng QE, Liu F, Jin ZM. Elastohydrodynamic lubrication analysis of metal-on-metal hip  
23    implants with complex structures using the finite-element method. *Proc Inst Mech Eng Part*  
24    *J: J Eng Trib.* 2010;224:1007-1018.
- 25    10. Gao L, Fisher J, Jin Z. Effect of walking patterns on the elastohydrodynamic lubrication of  
26    metal-on-metal total hip replacements. *Proc Inst Mech Eng Part J: J Eng Trib.* 2011;225:515-  
27    525.
- 28    11. Meng QE, Liu F, Fisher J, Jin ZM. Effect of simplifications of bone and components  
29    inclination on the elastohydrodynamic lubrication modeling of metal-on-metal hip  
30    resurfacing prosthesis. *Proc Inst Mech Eng Part H: J Eng Med.* 2013;227:523-534.
- 31    12. Meng QE, Liu F, Fisher J, Jin ZM. Contact mechanics and lubrication analyses of ceramic-  
32    on-metal total hip replacements. *Tribol Int.* 2013;63:51-60.
- 33    13. Sonntag R, Reinders J, Rieger JS, Heitzmann DWW, Kretzer JP. Hard-on-hard lubrication  
34    in the artificial hip under dynamic loading conditions. *PLoS One.* 2013;8:e71622.
- 35    14. Al-Hajjar M, Fisher J, Williams S, Tipper JL, Jennings LM. Effect of femoral head size on  
36    the wear of metal on metal bearings in total hip replacements under adverse edge-loading  
37    conditions. *J Biomed Mater Res B.* 2013;101B:213-222.
- 38    15. Goldsmith AAJ, Dowson D, Isaac GH, Lancaster JG. A comparative joint simulator study of  
39    the wear of metal-on-metal and alternative material combinations in hip replacements. *Proc*  
40    *Inst Mech Eng Part H: J Eng Med.* 2000;214:39-47.
- 41    16. Gao LM, Meng QE, Liu F, Fisher J, Jin ZM. The effect of aspherical geometry and surface  
42    texturing on the elastohydrodynamic lubrication of metal-on-metal hip prostheses under  
43    physiological loading and motions. *Proc Inst Mech Eng Part C: J Mech Eng Sci.*  
44    2010;224:2627-2636.

17. Meng QE, Gao LM, Liu F, Yang PR, Fisher J, Jin ZM. Contact mechanics and elastohydrodynamic lubrication in a novel metal-on-metal hip implant with an aspherical bearing surface. *J Biomech.* 2010;43:849-857.
18. Meng Q, Gao L, Liu F, Yang PR, Fisher J, Jin ZM. Transient elastohydrodynamic lubrication analysis of a novel metal-on-metal hip prosthesis with an aspherical acetabular bearing surface. *J Med Biomech.* 2009;24:352-361.
19. Liu F, Jin ZM, Hirt F, Rieker C, Roberts P, Grigoris P. Effect of wear of bearing surfaces on elastohydrodynamic lubrication of metal-on-metal hip implants. *Proc Inst Mech Eng Part H: J Eng Med.* 2005;219:319-328.
20. Kang L, Galvin AL, Fisher J, Jin ZM. Enhanced computational prediction of polyethylene wear in hip joints by incorporating cross-shear and contact pressure in addition to load and sliding distance: Effect of head diameter. *J Biomech.* 2009;42:912-918.
21. Liu F, Fisher J, Jin ZM. Effect of motion inputs on the wear prediction of artificial hip joints. *Tribol Int.* 2013;63:105-114.
22. Mattei L, Di Puccio F, Piccigallo B, Ciulli E. Lubrication and wear modelling of artificial hip joints: A review. *Tribol Int.* 2011;44:532-549.
23. Uddin MS, Zhang LC. Predicting the wear of hard-on-hard hip joint prostheses. *Wear.* 2013;301:192-200.
24. Brown TD, Lundberg HJ, Pedersen DR, Callaghan JJ. Clinical biomechanics of third body acceleration of total hip wear. *Clin Orthop Relat R.* 2009;467:1885-1897.
25. Liu F, Leslie I, Williams S, Fisher J, Jin Z. Development of computational wear simulation of metal-on-metal hip resurfacing replacements. *J Biomech.* 2008;41:686-694.
26. Puccio FD, Mattei L. A novel approach to the estimation and application of the wear coefficient of metal-on-metal hip implants. *Tribol Int.* 2015;83:69-76.
27. Archard JF. Contact and rubbing of flat surfaces. *J Appl Phys.* 1953;24:981-988.
28. Bowsher JG, Clarke IC, Williams PA, Donaldson TK. What is a "normal" wear pattern for metal-on-metal hip bearings? *J Biomed Mater Res B.* 2009;91B:297-308.
29. Leslie I, Williams S, Brown C, Isaac G, Jin ZM, Ingham E, Fisher J. Effect of bearing size on the long-term wear, wear debris, and ion levels of large diameter metal-on-metal hip replacements - An in vitro study. *J Biomed Mater Res B.* 2008;87B:163-172.
30. Williams S, Stewart TD, Ingham E, Stone MH, Fisher J. Metal-on-metal bearing wear with different swing phase loads. *J Biomed Mater Res B.* 2004;70B:233-239.
31. Dowson D, Neville A. Tribology and corrosion in hip joint replacements: materials and engineering. Revell PA, editor. *Joint Replacement Technology.* Second Edition. Cambridge: Woodhead Publishing; 2014: 401-442.
32. Dowson D. The relationship between steady-state wear rate and theoretical film thickness in metal-on-metal total replacement joints. *Proceedings of the 29th Leeds-Lyon Symposium on Tribology;* 2003; Leeds, UK: Elsevier.
33. Dowson D. Tribological principles in metal-on-metal hip joint design. *Proc Inst Mech Eng Part H: J Eng Med.* 2006;220:161-171.
34. Dowson D, Hardaker C, Flett M, Isaac GH. A hip joint simulator study of the performance of metal-on-metal joints. Part II: Design. *J Arthroplasty.* 2004;19:124-130.
35. Paré P, Medley JB, Chan FW, Young SK. On the role of the lambda parameter in simulator wear of metal-on-metal hip implants. *Proceedings of the 29th Leeds-Lyon Symposium on Tribology International;* 2003; Leeds, UK: Elsevier.

36. Hesketh J, Meng Q, Dowson D, Neville A. Biotribocorrosion of metal-on-metal hip replacements: How surface degradation can influence metal ion formation. *Tribol Int.* 2013;65:128-137.
37. Catelas I, Bobyn JD, Medley JJ, Zukor DJ, Petit A, Huk OL. Effects of digestion protocols on the isolation and characterization of metal-metal wear particles. II. Analysis of ion release and particle composition. *J Biomed Mater Res.* 2001;55:330-337.
38. Daniel J, Holland J, Quigley L, Sprague S, Bhandari M. Pseudotumors associated with total hip arthroplasty. *J Bone Joint Surg Am.* 2012;94A:86-93.
39. Liu A, Richards L, Bladen CL, Ingham E, Fisher J, Tipper J. The biological response to nanometre-sized polymer particles. *Acta Biomater.* 2015;23:38-51.
40. Madl AK, Liong M, Kovochich M, Finley BL, Paustenbach DJ, Oberdorster G. Toxicology of wear particles of cobalt-chromium alloy metal-on-metal hip implants Part I: Physicochemical properties in patient and simulator studies. *Nanomedicine: NBM.* 2015;11:1201-1215.
41. Prostheses used in hip, knee, ankle, elbow and shoulder replacement procedures 2012. National Joint Registry, 2013.
42. Hart AJ, Sabah SA, Henckel J, Lloyd G, Skinner JA. Lessons learnt from metal-on-metal hip arthroplasties will lead to safer innovation for all medical devices. *Hip Int.* 2015;25:347-354.
43. Dowson D. New joints for the Millennium: wear control in total replacement hip joints. *Proc Inst Mech Eng Part H: J Eng Med.* 2001;215:335-358.
44. Sharif KJ, Evans HP, Snidle RW, Barnett D, Egorov IM. Effect of elastohydrodynamic film thickness on a wear model for worm gears. *Proc Inst Mech Eng Part J: J Eng Trib.* 2006;220:295-306.
45. Cooke AV, Dowson D, Wright V. The rheology of synovial fluid and some potential synthetic lubricants for degenerate synovial fluid. *Proc Inst Mech Eng Part H: J Eng Med.* 1978;7:66-72.
46. Yao JQ, Laurent MP, Johnson TS, Blanchard CR, Crowninshield RD. The influences of lubricant and material on polymer/CoCr sliding friction. *Wear.* 2003;255:780-784.
47. Gao L, Dowson D, Hewson RW. A numerical study of non-Newtonian transient elastohydrodynamic lubrication of metal-on-metal hip prostheses. *Tribol Int.* in press.
48. Dowson D, McNie CM, Goldsmith AAJ. Direct experimental evidence of lubrication in a metal-on-metal total hip replacement tested in a joint simulator. *Proc Inst Mech Eng Part C: J Mech Eng Sci.* 2000;214:75-86.
49. Myant C, Underwood R, Fan J, Cann PM. Lubrication of metal-on-metal hip joints: The effect of protein content and load on film formation and wear. *J Mech Behav Biomed.* 2012;6:30-40.
50. Wang FC, Jin ZM. Prediction of elastic deformation of acetabular cups and femoral heads for lubrication analysis of artificial hip joints. *Proc Inst Mech Eng Part J: J Eng Trib.* 2004;218:201-209.
51. Venner CH, Lubrecht AA. Multigrid techniques: a fast and efficient method for the numerical simulation of elastohydrodynamically lubricated point contact problems. *Proc Inst Mech Eng Part J: J Eng Trib.* 2000;214:43-62.
52. Parkes M, Myant C, Cann PM, Wong JSS. The effect of buffer solution choice on protein adsorption and lubrication. *Tribol Int.* 2014;72:108-117.
53. Alvarez-Vera M, Ortega-Saenz JA, Hernandez-Rodriguez MAL. A study of the wear performance in a hip simulator of a metal-metal Co-Cr alloy with different boron additions. *Wear.* 2013;301:175-181.

54. Bowsher JG, Hussain A, Williams PA, Shelton JC. Metal-on-metal hip simulator study of increased wear particle surface area due to 'severe' patient activity. Proc Inst Mech Eng Part H: J Eng Med. 2006;220:279-287.
55. Calonijs O, Saikko V. Slide track analysis of eight contemporary hip simulator designs. J Biomech. 2002;35:1439-1450.

## Figure captions

**FIGURE 1.** Representation of typical physical simulator wear results

**FIGURE 2.** Illustration of the effect of the power term ( $\alpha$ ) in the wear formula ( $R_a = 40$  nm)

**FIGURE 3.** Flowchart of wear simulation procedure

**FIGURE 4.** Illustration of a metal-on-metal hip bearing

**FIGURE 5.** Load (A) and angular velocity (B) in gait cycles of the ProSim hip simulator

**FIGURE 6.** Scalability of wear coefficient on the predicted wear volume (A) and wear depth

(B); Head 36; power term  $\alpha = 2.24$ .

**FIGURE 7.** Effect of the power term ( $\alpha$ ) on the accumulated wear volume (A) and maximum

wear depth (B); Head 36; wear coefficient  $k_w = 1 \times 10^{-9} \text{mm}^3/(\text{Nm})$ .

**FIGURE 8.** Accumulated wear and maximum wear depth of Head 36 (A and B) and Head 28

(C and D) bearings; power term  $\alpha = 2.24$ ; wear coefficient  $k_w = 1 \times 10^{-9} \text{mm}^3/(\text{Nm})$ .

**FIGURE 9.** Wear scar on cup (A and B) and head (C and D); Head 36; power term  $\alpha = 2.24$ ; wear coefficient  $k_w = 1 \times 10^{-9} \text{mm}^3/(\text{Nm})$ . (Horizontal axis is azimuthal angle and vertical axis is polar angle with both unit of degrees; MC = Million Cycles.)

**FIGURE 10.** Time averaged pressure distribution (A) and film thickness distribution (B) along

the cross-section line as shown in Figure 4 (dash line). The value is averaged over a walking

cycle time; Head 36; power term  $\alpha = 2.24$ ; wear coefficient  $k_w = 1 \times 10^{-9} \text{mm}^3/(\text{Nm})$ .

**TABEL I.** Geometrical and material parameters of a MOM total hip replacement

Head diameter	28 and 36 mm
Diametrical clearance	40 and 50 $\mu\text{m}$
Cup wall thickness	9.5 mm
Equivalent support thickness	2 mm
Elastic modulus of metal	210 GPa
Elastic modulus of equivalent support	2.27 GPa
Poisson's ratio of metal	0.3
Poisson's ratio of equivalent support	0.23
Viscosity of synovial fluid	0.0009 Pa s

**TABEL II.** Wear rate ( $\text{mm}^3/\text{MC}$ ) (based on Figure 8A and C; MC = Million Cycles)

Wear rate	1 <sup>st</sup> MC	2 <sup>nd</sup> MC	4 <sup>th</sup> MC	6 <sup>th</sup> MC	8 <sup>th</sup> MC	12 <sup>th</sup> MC	15 <sup>th</sup> MC
Head 36	0.0206	0.0179	0.0148	0.0130	0.0119	0.0105	0.0100
	100%	86.9%	71.8%	63.1%	57.8%	51.0%	48.5%
Head 28	0.0302	0.0246	0.0207	0.0183	0.0154	0.0099	0.0085
	100%	81.5%	68.5%	60.6%	51.0%	32.8%	28.1%

## Figures

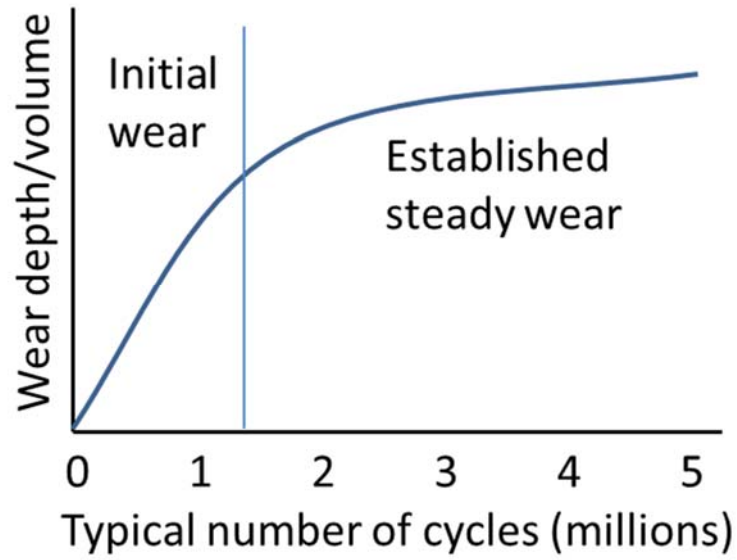


**FIGURE 1.** Representation of typical physical simulator wear results

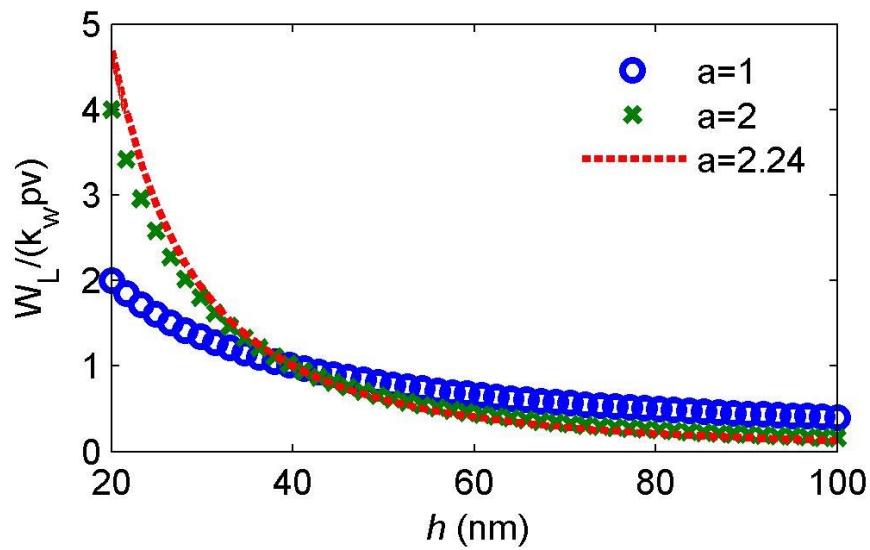


**FIGURE 2.** Illustration of the effect of the power term ( $a$ ) in the wear formula ( $R_o = 40$  nm)

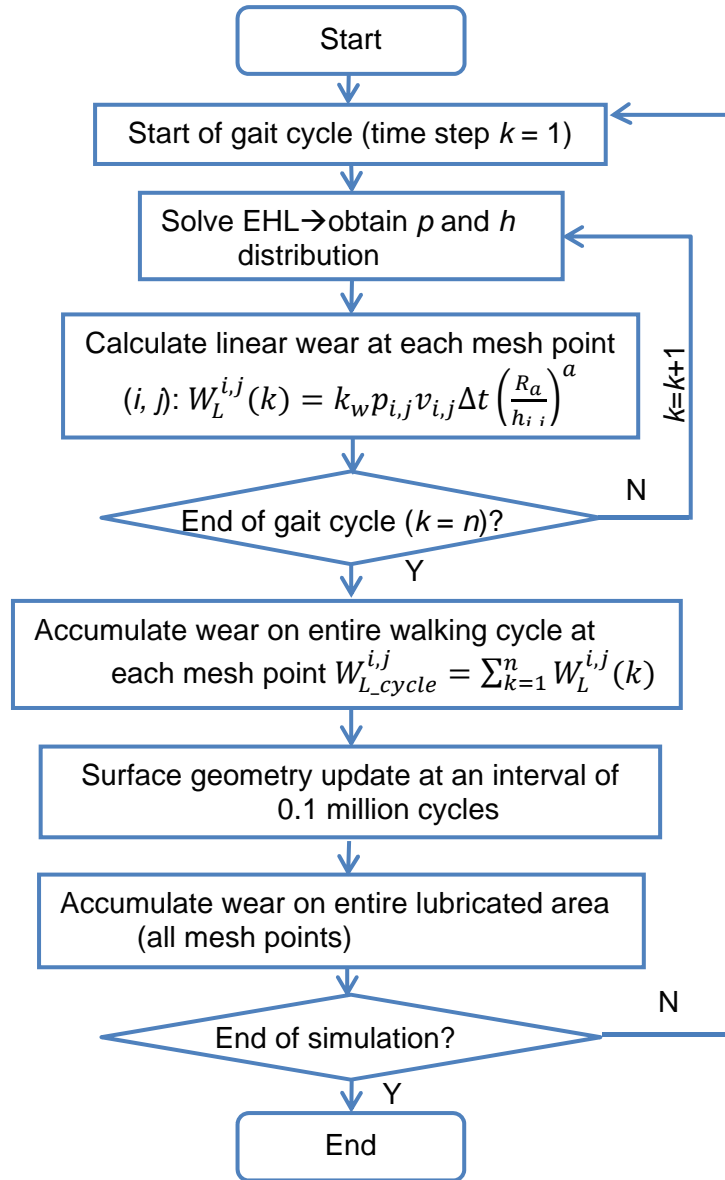


**FIGURE 3.** Flowchart of wear simulation procedure



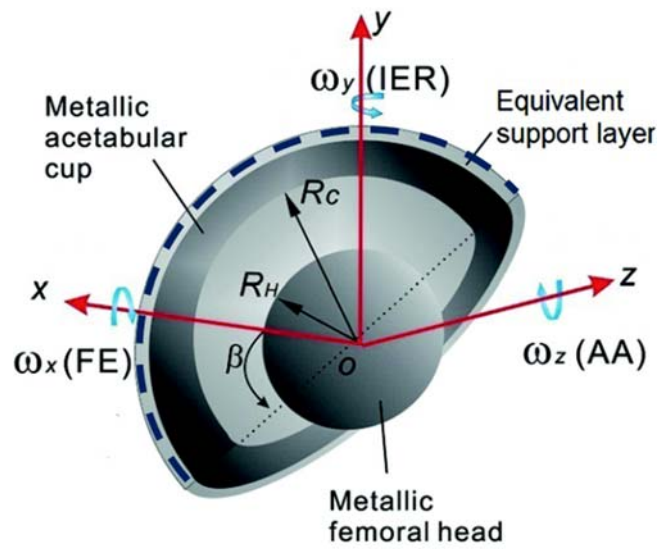


**FIGURE 4.** Illustration of a metal-on-metal hip bearing

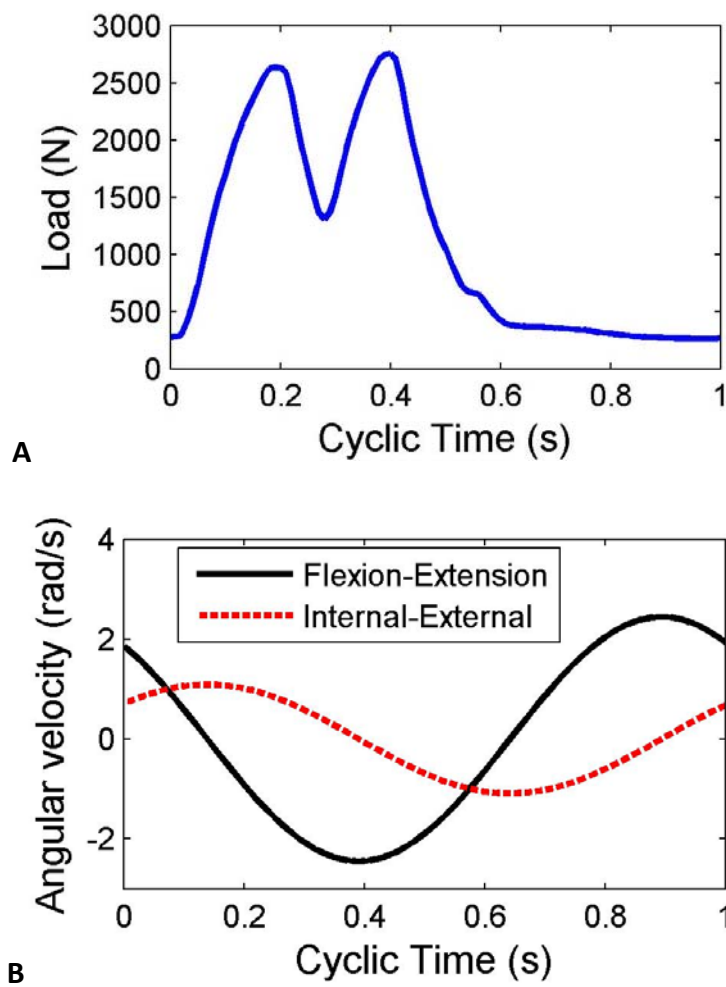


**FIGURE 5.** Load (A) and angular velocity (B) in gait cycles of the ProSim hip simulator

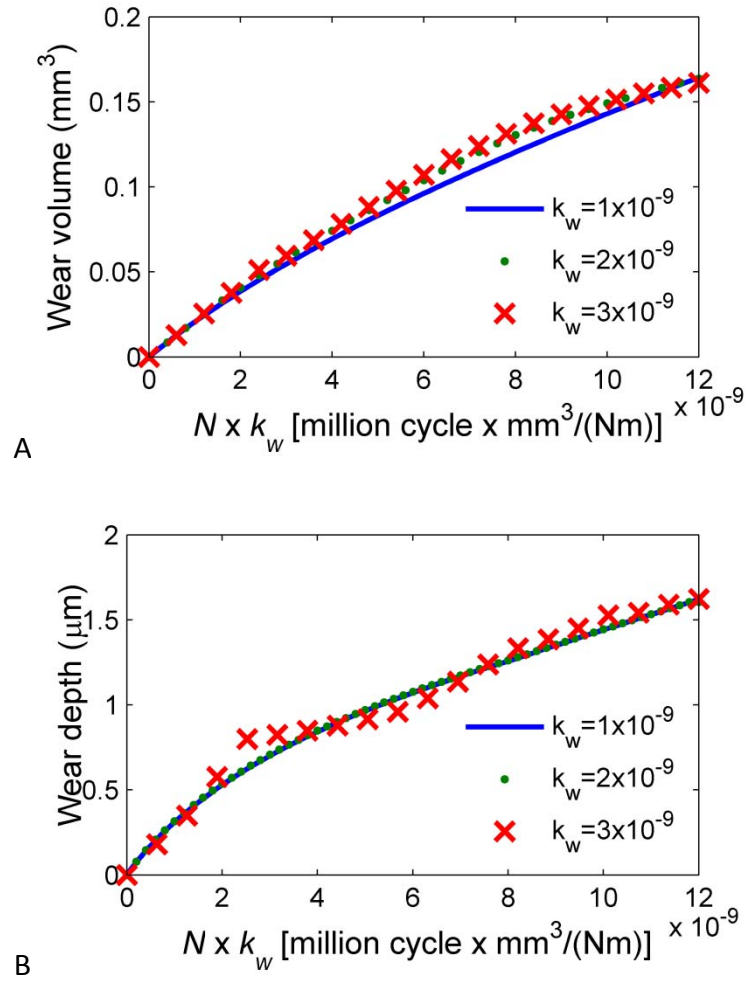


**FIGURE 6.** Scalability of wear coefficient on the predicted wear volume (A) and wear depth (B); Head 36; power term  $a = 2.24$ ; wear coefficient  $k_w = 1 \times 10^{-9} \sim 3 \times 10^{-9} \text{mm}^3/(\text{Nm})$ .

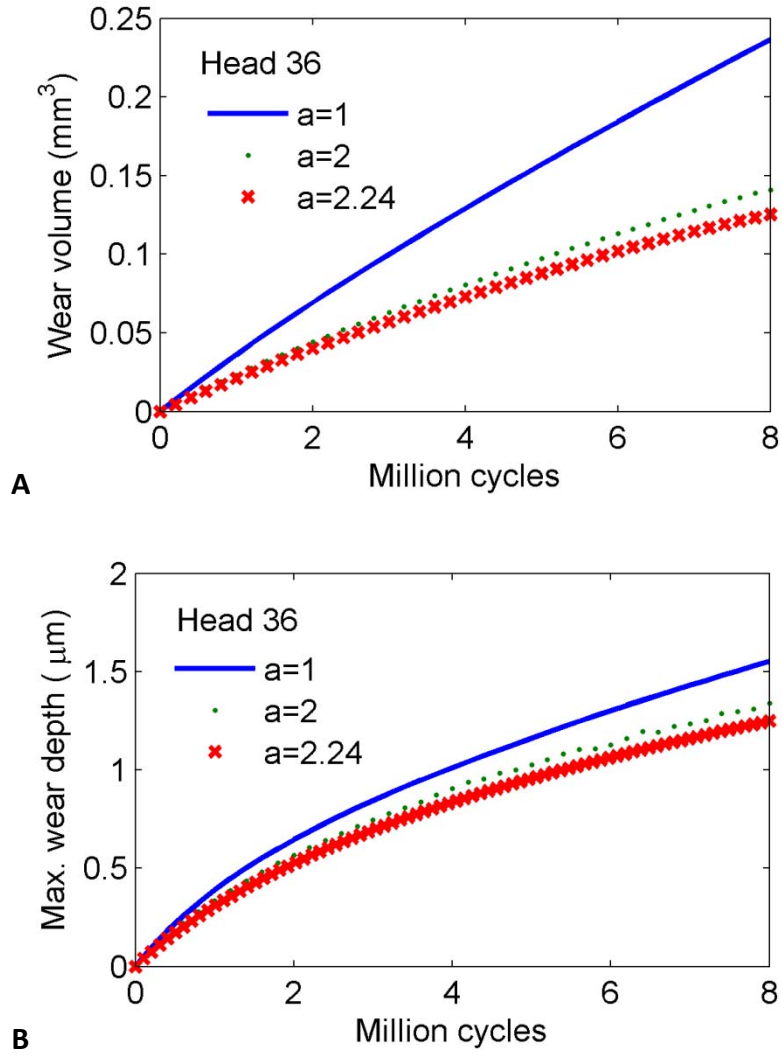
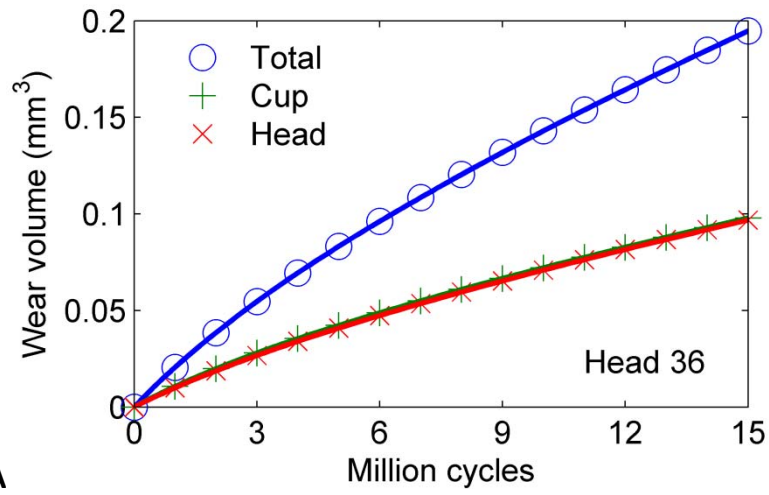
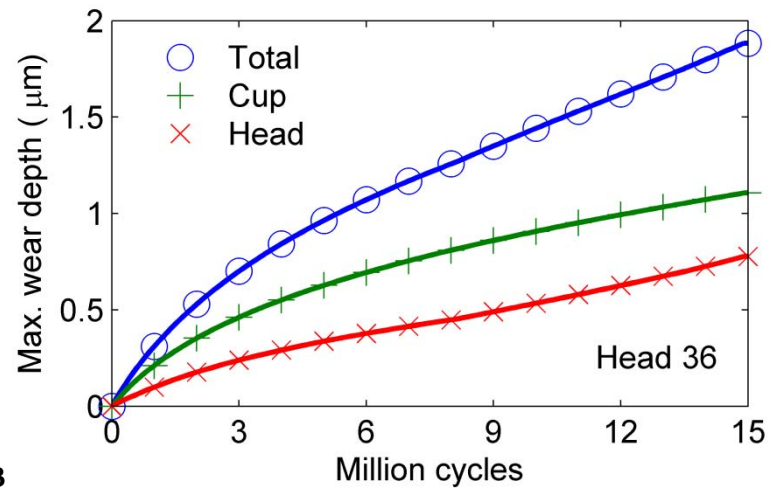


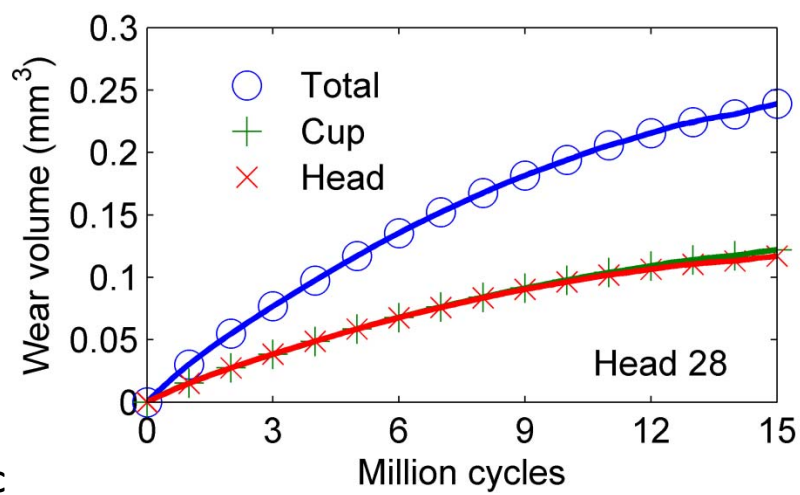
**FIGURE 7.** Effect of the power term ( $a$ ) on the accumulated wear volume (A) and maximum wear depth (B); Head 36; power term  $a = 1, 2$  and  $2.24$ ; wear coefficient  $k_w = 1 \times 10^{-9} \text{mm}^3/(\text{Nm})$ .



A



B



C

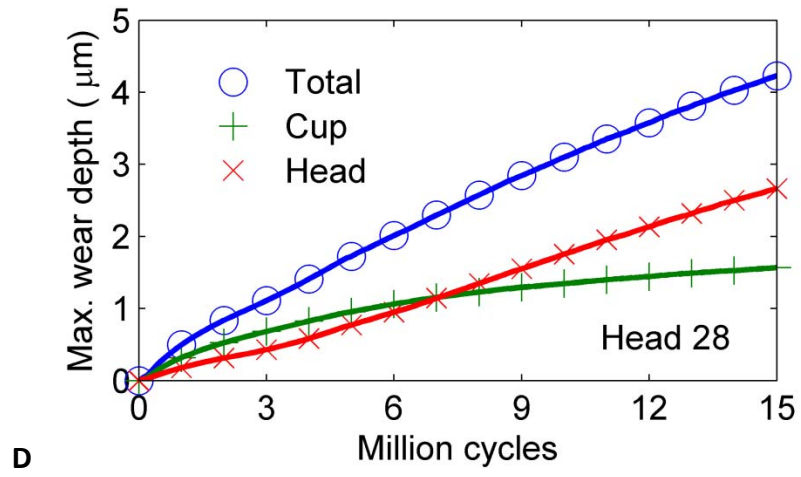


**FIGURE 8.** Accumulated wear and maximum wear depth of Head 36 (A and B) and Head 28 (C and D) bearings; power term  $\alpha = 2.24$ ; wear coefficient  $k_w = 1 \times 10^{-9} \text{mm}^3/(\text{Nm})$ .

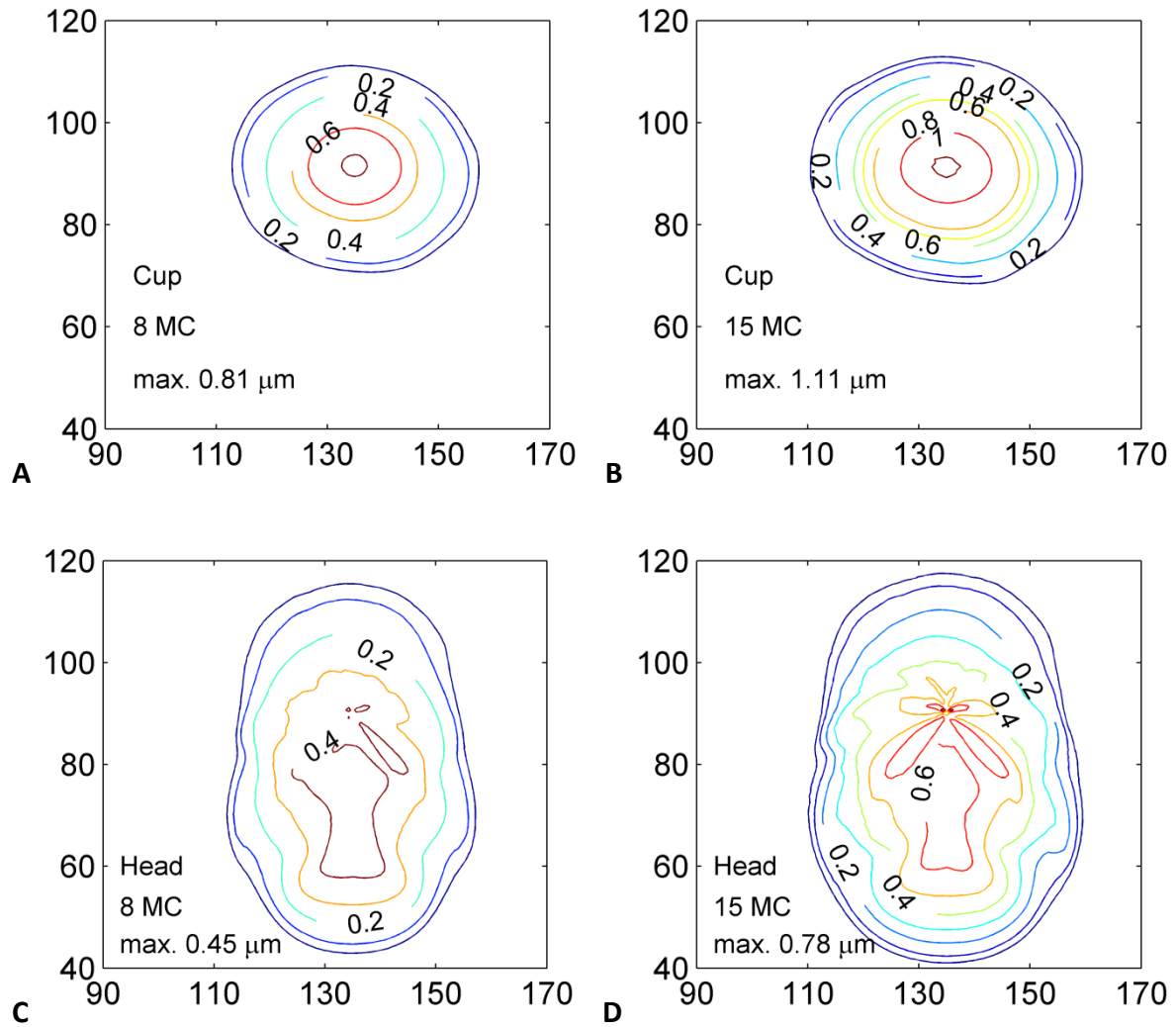


**FIGURE 9.** Wear scar on cup (A and B) and head (C and D) surfaces; Head 36; power term  $\alpha = 2.24$ ; wear coefficient  $k_w = 1 \times 10^{-9} \text{mm}^3/(\text{Nm})$ . (Horizontal axis is azimuthal angle and vertical axis is polar angle with both unit of degrees; MC = Million Cycles.)

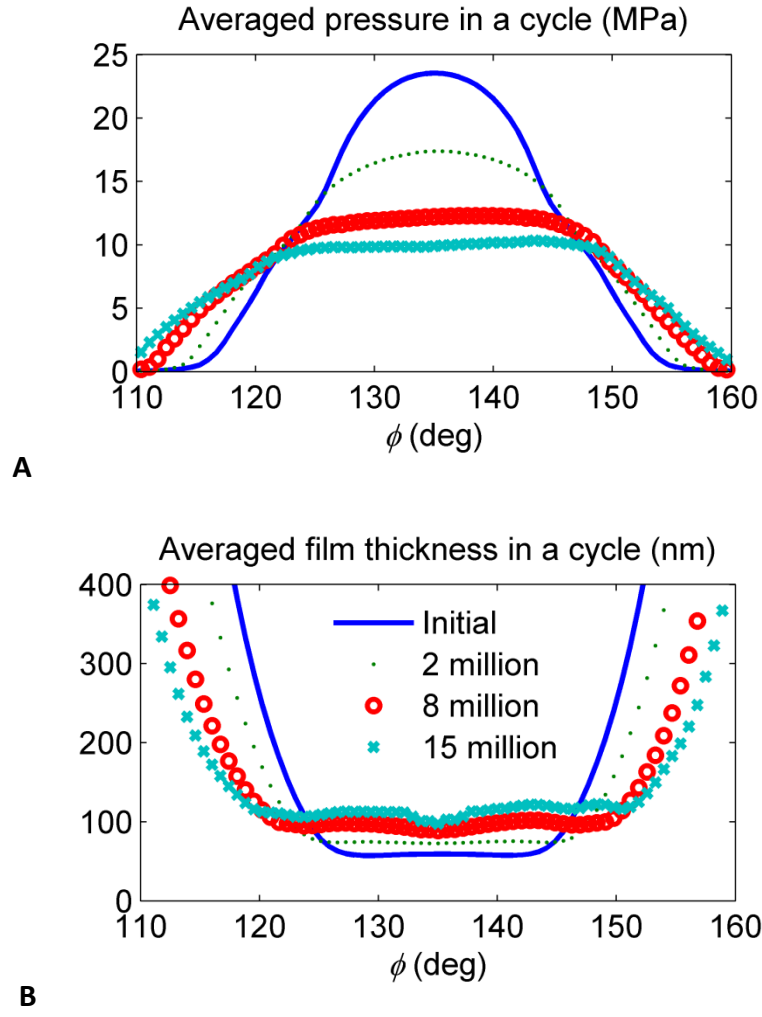


**FIGURE 10.** Time averaged pressure distribution (A) and film thickness distribution (B) along the cross-section line as shown in Figure 4 (dash line). The value is averaged over a walking cycle time; Head 36; power term  $a = 2.24$ ; wear coefficient  $k_w = 1 \times 10^{-9} \text{mm}^3/(\text{Nm})$ .